# Highly structured slow solar wind emerging from an equatorial coronal hole

S. D. Bale[1,2,3,4*], S. T. Badman[1,2], J. W. Bonnell[1], T. A. Bowen[1], D. Burgess[4], A. W. Case[5], C. A. Cattell[6], B. D. G. Chandran[7,8], C. C. Chaston[1], C. H. K. Chen[4], J. F. Drake[9,10,11], T. Dudok de Wit[12], J. P. Eastwood[3], R. E. Ergun[13], W. M. Farrell[14], C. Fong[1,2], K. Goetz[6], M. Goldstein[15,16], K. A. Goodrich[1], P. R. Harvey[1], T. S. Horbury[3], G. G. Howes[17], J. C. Kasper[18,5], P. J. Kellogg[6], J. A. Klimchuk[19], K. E. Korreck[5], V. V. Krasnoselskikh[12], S. Krucker[1,20], R. Laker[3], D. E. Larson[1], R. J. MacDowall[14], M. Maksimovic[21], D. M. Malaspina[13], J. Martinez-Oliveros[1], D. J. McComas[22], N. Meyer-Vernet[21], M. Moncuquet[21], F. S. Mozer[1], T. D. Phan[1], M. Pulupa[1], N. E. Raouafi[23], C. Salem[1], D. Stansby[3], M. Stevens[5], A. Szabo[19], M. Velli[24], T. Woolley[3], J. R. Wygant[6]

[1]Space Sciences Laboratory, University of California, Berkeley, CA 94720-7450, USA
[2]Physics Department, University of California, Berkeley, CA 94720-7300, USA
[3]The Blackett Laboratory, Imperial College London, London, SW7 2AZ, UK
[4]School of Physics and Astronomy, Queen Mary University of London, London E1 4NS, UK
[5]Smithsonian Astrophysical Observatory, Cambridge, MA 02138 USA
[6]School of Physics and Astronomy, University of Minnesota, Minneapolis, MN 55455
[7]Department of Physics & Astronomy, University of New Hampshire, Durham, NH 03824, USA
[8]Space Science Center, University of New Hampshire, Durham, NH 03824, USA
[9]Department of Physics, University of Maryland, College Park, MD 20742, USA
[10]Institute for Physical Science and Technology, University of Maryland, College Park, MD 20742, USA
[11]Joint Space Science Institute, University of Maryland, College Park, MD 20742, USA
[12]LPC2E, CNRS and University of Orléans, Orléans, France
[13]Laboratory for Atmospheric and Space Physics, University of Colorado, Boulder, CO 80303, USA
[14]Code 695, NASA Goddard Space Flight Center, Greenbelt, MD 20771, USA
[15]Goddard Planetary Heliophysics Institute, University of Maryland Baltimore County, Baltimore, MD 21250, USA
[16]Code 672, NASA Goddard Space Flight Center, Greenbelt, MD 20771, USA
[17]Department of Physics and Astronomy, University of Iowa, Iowa City, IA 52242, USA
[18]Climate and Space Sciences and Engineering, University of Michigan, Ann Arbor, MI 48109, USA
[19]Heliophysics Division, NASA Goddard Space Flight Center, Greenbelt, MD 20771, USA
[20]University of Applied Sciences and Arts Northwestern Switzerland, 5210 Windisch, Switzerland
[21]LESIA, Observatoire de Paris, Université PSL, CNRS, Sorbonne Université, 92195 Meudon, France
[22]Department of Astrophysical Sciences, Princeton University, Princeton, NJ 08544, USA
[23]Johns Hopkins University Applied Physics Laboratory, Laurel, MD, USA
[24]Department of Earth, Planetary, and Space Sciences, University of California, Los Angeles, USA

* email: bale@berkeley.edu

**At solar minimum, the solar wind[1,2] is observed at high solar latitudes as a predominantly fast (> 500 km/s), highly Alfvenic, rarefied stream of plasma originating deep within coronal holes, while near the ecliptic plane it is interspersed with a more variable slow (< 500 kms) wind[3]. The precise origins of the slow wind streams are less certain[4], with theories and observations supporting sources from the tips of helmet streamers[5,6], interchange reconnection near coronal hole boundaries[7,8], and origins within coronal holes with highly diverging magnetic fields[9,10]. The heating mechanism required to drive the solar wind is also an open question and candidate mechanisms include Alfven wave turbulence[11,12], heating by reconnection in nanoflares[13], ion cyclotron wave heating[14] and acceleration by thermal gradients[1]. At 1 au,**

**the wind is mixed and evolved and much of the diagnostic structure of these sources and processes has been lost. Here we present new measurements from Parker Solar Probe[15] at 36 to 54 solar radii that show clear evidence of slow, Alfvenic solar wind emerging from a small equatorial coronal hole. The measured magnetic field exhibits patches of large, intermittent reversals associated with jets of plasma and enhanced Poynting flux and interspersed in a smoother and less turbulent flow with near-radial magnetic field. Furthermore, plasma wave measurements suggest electron and ion velocity-space micro-instabilities[16,10] that have been identified with plasma heating and thermalization processes. Our measurements suggest an impulsive mechanism associated with solar wind energization and a heating role for micro-instabilities and provide strong evidence for low latitude coronal holes as a significant contribution to the source of the slow solar wind.**

**Magnetic Field Structure:** The first solar encounter (E1) of Parker Solar Probe occurred during solar minimum, the spacecraft orbit remained within 5° of the heliographic solar equator and unlike any previous spacecraft, was co-rotational with the Sun for two intervals surrounding perihelion. Figure 1 summarizes the radial magnetic field ($B_R$) structure observed by the FIELDS experiment[17] for a six-week time interval centered on perihelion (November 6, 2018). Panel (a) shows 1 second cadence measurements of $B_R$ (see Methods) which show the overall $1/r^2$ behavior expected from simple flux-conservation arguments[18] as PSP's heliocentric distance varied along its eccentric orbit. Upon this background, dramatic and unexpected rapid polarity reversals of order $\delta B_R/|B| \sim 1$ are superposed. One-hour statistical modes (most probable value – see Methods) of $B_R$ in Fig. 1b remove the transient polarity inversions and reveal the large-scale magnetic structure. Time series predictions of $B_R$ generated from the simple, but widely used, Potential Field Source Surface (PFSS) model[19,20,21] are shown for comparison in black and green. The implementation of this model and the procedure to connect it to the location of PSP and generate time series is discussed in the Methods section.

PFSS is a zero-current force free model of the global solar corona, meaning it assumes magnetic pressure dominates over gas pressure (low plasma beta) to such an extent that the problem reduces to magnetostatics, giving a solution of a static field configuration which rigidly corotates with the sun. The role of gas dynamics is approximated by requiring the tangential field vanishes at a spherical "source surface" of some radius $R_{SS}$, which simulates how the outflowing solar wind drags the field lines out into the heliosphere. The magnetostatic approximation limits the accuracy and applicability of the model. Nevertheless, PFSS is widely used as a computationally tractable first approximation and forms the basis for the more sophisticated models[21,22]. We note that PSP E1 took place very close to solar minimum, with low solar activity low, reducing the impact of non-potential transient events and active regions.

In Fig 1b, two model evaluations are shown with $R_{SS}$ = 2.0 Rs (green) and $R_{SS}$ = 1.2Rs (black respectively. In both cases $R_{SS}$ is well below the canonical value[23] but is necessary to provide good agreement for all model inputs (see Methods) and is not without precedent[24,25]. Model comparison reveals an overall very good agreement for both models, but also shows the polarity inversions at features A and C are washed out except with the lower source surface height (black line). Meanwhile the timing of feature G is better captured with the higher source surface height (green), illustrating the difficulty PFSS has with assuming a *single* source surface height and supports previous findings of a varying “true” source surface height[25,26]. Finally, Fig 1. (c) and (d) depict field line mappings derived from the same PFSS models shown in panel (b) to connect the spacecraft down to the lower corona to establish context for the *in situ* measurements. The spacecraft trajectory is shown projected onto the source surface colored by its measured polarity. The background is a synoptic map of EUV emission in the 171Å wavelength for which dark regions imply lower density plasma and the likely location of open magnetic field lines. This background is shown in isolation in Extended Data Figure 4 along with its corresponding map for the 193Å wavelength for the readers reference. The neutral lines derived from the PFSS models are shown as single contours in the same color as their time series in Fig. 1(b). Panel (c) shows how the neutral line topology explains the polarity inversions measured by PSP. Panel (d) zooms in to the 2-week interval closest to perihelion (330° longitude). During the entire 2-week co-rotation loop period, PSP remained connected to a small, negative polarity, isolated equatorial coronal hole, suggesting the rapid magnetic field polarity reversals seen in Fig. 1a are magnetic structures emerging from this coronal hole and sweeping past the PSP spacecraft. Extended Data Figure 5 indicates the configuration schematically. For most of this interval, SWEAP[27] measurements of the solar wind velocity indicated an Alfvenic slow wind stream (see Fig 2. below), suggesting a significant slow wind source rooted in equatorial coronal holes at the Sun. Polarity inversions *B* and *E* are associated with (transient) fluxrope and coronal mass ejection[28] events, respectively.

**Alfvenic Fluctuations and Plasma Jets:** Time series magnetic field and velocity structures show the correlations (Fig. 2c, 2d, and 2e) expected of propagating Alfvén waves[29], especially during the quiet, radial field intervals. The $\delta B_R$ polarity reversal intervals show enhanced radial wind velocity (Fig. 2e) and the Alfvénic correlations ($\delta v$ to $\delta B$) within the polarity inversions and jets suggest that these structures may be interpreted as large amplitude, 3D Alfvénic structures convected away from the Sun. As a simple measure, statistics of zero-crossings (polarity reversals – see Methods) show that ~6% of the temporal duration of E1 is comprised of jets, so defined. Many jet intervals show signatures of compressibility (Fig. 2a), in this case anti-correlated plasma density $n_e$ and magnetic field magnitude |B| suggesting slow-mode or pressure-balanced behavior[30]. While isolated Alfvénic features associated with magnetic field reversals have been identified at 60 $R_S$[31], near 1 au[32] and in the polar heliosphere by Ulysses[33], at those greater distances little or no compressive signatures were present. It has been suggested[34] that these magnetic structures could be signatures of impulsive reconnection events in the Sun’s atmosphere[35]; simulations[36] show qualitative similarities to the E1 events but do not reproduce the observed magnetic field reversals past 90°.

Alfvénic structures and waves have long been considered to be an important energy source for the wind[11,12]. The radial Poynting flux $S_R = ExB/\mu_0$ (see Methods) in the spacecraft frame (Fig. 2b) is ~10% of the kinetic energy flux (blue curve) and shows enhancements during the jet intervals, suggesting that these plasma jets may impart energy to the emerging solar wind. As seen in Fig. 1a and Fig. 2e, the plasma jets appear to be clustered and interspersed in an otherwise quiet solar wind flow with prominently radial magnetic field.

**Micro-instabilities and Turbulence:** The quiet radial flow intervals contain plasma waves consistent with expectations of micro-instabilities associated with ion[14] and electron[16] velocity-space structure (Fig. 3). The electric field spectrum from ~11 to ~1688 kHz, shows signatures of plasma quasi-thermal noise[37] (Fig. 3a) at the electron plasma frequency $f_{pe}$ (used to estimate the total plasma density in Fig. 2a). Intense bursts of narrowband, electrostatic Langmuir waves (Fig. 3a) occur throughout the perihelion encounter; narrowband Langmuir waves are driven by electron beams and damp rapidly, suggesting the presence of an intermittent, local population of electron beams.

The electric field spectrum (Fig. 3b) from 0.3 to ~75 kHz shows intermittent bursts of electrostatic whistler wave activity, peaked in power below the electron gyrofrequency $f_{ce}$. Also present are waves containing harmonic structure consistent with electron Bernstein wave emission. Electrostatic whistler/Bernstein bursts[16] are generated by features in the electron velocity distribution function $f_e(v)$ and are not observed in the solar wind at 1 au. Here they occur only in the quiet radial field intervals. A wavelet spectrogram (divided by $P_K \sim f^{-5/3}$) of search coil magnetometer and fluxgate magnetometer data in Fig. 3c shows the spectral content of the magnetic field to ~146 Hz. A spectral break between 1-10 Hz (in the spacecraft frame) is highly variable and associated with the transition from a magnetohydrodynamic (MHD) turbulent cascade to dissipation and/or dispersion ranges at ion kinetic length scales[38]. Note that overall turbulent levels are lower and more intermittent in the quiet radial wind (Fig. 3c and Fig. 4a). The spectrum of magnetic helicity $\sigma_m$[39] in Fig. 3d indicates intervals of large ($1 > \sigma_m > 0.5$ in red, $-0.5 < \sigma_m < -1$ in blue) circular polarization often associated with ion cyclotron (IC) waves[040]. These ion wave events are apparent during quiet, radial field intervals.

The (trace) magnetic field spectra (see Methods), averaged over 30 minutes (upper panel Fig. 4), show broken power-law behavior, with spectral indices roughly comparable to the -5/3 and -8/3 predictions for MHD and kinetic scale turbulence[38], respectively. This suggests that by 36.6 Rs, the solar wind has already developed a turbulent cascade to transport energy from large scale motions to the micro-scales where it can be dissipated. In the radial quiet wind (blue), where the turbulence level is significantly lower, an enhancement of wave power near the ion cyclotron frequency is observed. In the active jet wind (black), a steep spectrum is seen at the plasma ion inertial and gyroscales, indicating a transition to kinetic range turbulence and possibly the dissipation of turbulent energy to heat the solar wind as it expands to fill the heliosphere. In both types of wind, the power levels are several orders of magnitude larger than at 1 au. The magnetic compressibility[41], defined as $C_{bb} = (\delta|B|/|\delta B|)^2$ shows an increase at high frequencies as expected for kinetic range turbulence (lower panel Fig. 4). At low frequencies, the compressibility is larger in jet wind than in quiet wind, but remains small, $C_{bb} <\sim 0.1$, indicating that jet fluctuations have an enhanced compressible component but are still predominantly Alfvenic[41]. In the quiet wind, the band of enhanced power near the cyclotron frequency has a reduced magnetic compressibility as expected for quasi-parallel ion cyclotron waves[40]. PSP Encounter 1 reveals a more structured and dynamic solar wind than is seen at 1 au, with impulsive, magnetic-field reversals and plasma jets embedded in a quiet radial wind emerging from a small equatorial coronal hole. As PSP goes to lower altitudes, eventually to 9.8 $R_S$, during the upcoming solar maximum, we expect to descend below the Alfvén surface and measure the interface between the corona and the solar wind for the first time.

**Data Availability** The data used in this study are available from November 12, 2019 at the NASA Space Physics Data Facility (SPDF).

# References

[1]Parker, E. N., Dynamics of the Interplanetary Gas and Magnetic Fields., *The Astrophysical Journal,* 128, 664., 1958.
[2]Neugebauer, M. and Snyder, C. W., Solar Plasma Experiment., *Science*, 138, 109, 1962.
[3]McComas, D. J., et al., Weaker solar wind from the polar coronal holes and the whole Sun. *Geophysical Research Letters* 35, L18103, 2008.
[4]Abbo, L., et al., Slow Solar Wind: Observations and Modeling. *Space Science Reviews,* 201, 55, 2016
[5]Lapenta, G., and Knoll, D.A., Effect of a Converging Flow at the Streamer Cusp on the Genesis of the Slow Solar Wind., *The Astrophysical Journal*, 624, 1049, 2005.
[6]Einaudi, G., Boncinelli, P., Dahlburg, R.B., and Karpen, J.T., 1999, Formation of the slow solar wind in a coronal streamer., *J. Geophys. Res*., 104, 521, 1999.
[7]Fisk, L.A., and Schwadron, N.A., The Behavior of the Open Magnetic Field of the Sun., *The Astrophysical Journal*, 560, 425, 2001.
[8]Antiochos, S.K., Mikic, Z., Titov, V.S., Lionello, R., and Linker, J.A., A Model for the Sources of the Slow Solar Wind., *The Astrophysical Journal*, 731, 112, 2011.
[9]Wang Y.-M. and N. R. Sheeley, On potential field models of the solar corona., *Astrophysical Journal*, v.392, p.310, 1992.
[10]Cranmer, S.R.: 2009, Coronal Holes., *Living Reviews in Solar Physics*, 6, 3, 2009.
[11]Hollweg, J.V., and Johnson, W., Transition region, corona, and solar wind in coronal holes: Some two-fluid models., *J. Geophys. Res*., 93, 9547, 1988.
[12]Verdini, A., Velli, M., Matthaeus, W.H., Oughton, S., and Dmitruk, P., A Turbulence-Driven Model for Heating and Acceleration of the Fast Wind in Coronal Holes., *The Astrophysical Journal*, 708, L116, 2010.
[13]Parker, E.N., Heating Solar Coronal Holes., *The Astrophysical Journal*, 372, 719, 1991.
[14]Cranmer, S.R., Field, G.B., and Kohl, J.L., Spectroscopic Constraints on Models of Ion Cyclotron Resonance Heating in the Polar Solar Corona and High-Speed Solar Wind., *The Astrophysical Journal*, 518, 937, 1999.
[15]Fox, N.J., et al., The Solar Probe Plus mission:  Humanity's first visit to our star., *Space Sci Rev*, 204: 7, 2016
[16]Breneman, A. W., et al, STEREO and Wind observations of intense cyclotron harmonic waves at the Earth's bow shock and inside the magnetosheath., *J. Geophys. Res. Space Physics*, 118, 7654– 7664, 2013.
[17]Bale, S.D, et al., The FIELDS Instrument Suite for Solar Probe Plus., *Space Sci Rev*, 204: 49, 2016.
[18]Parker, E. N., Dynamical Theory of the Solar Wind, *Space Science Reviews*, Volume 4, Issue 5-6, pp. 666-708, 1965
[19]Altschuler, M. D. and G. Newkirk, Magnetic Fields and Structure of the Solar Corona:  1.  Methods of Calculating Coronal Fields., *Solar Physics*, Volume 9, Issue 1, pp.131-149, 1969.
[20]Schatten, K. H., J. M. Wilcox, and N. F. Ness, A model of interplanetary and coronal magnetic fields., *Solar Physics*, 6:442-455, March 1969.
[21]Arge, C. N. and V. J. Pizzo, Improvement in the prediction of solar wind conditions using near-real time solar magnetic field updates., *J Geophys. Res: Space Physics*, 105(A5):10465-10479, 2000.
[22]Riley, P., J. A. Linker, Z. Mikic, R. Lionello, S. A. Ledvina, and J. G. Luhmann, A Comparison between Global Solar Magnetohydrodynamic and Potential Field Source Surface Model Results., *The Astrophysical Journal*, 653:1510-1516, 2006.
[23]Hoeksema, J. T., Structure and evolution of the large scale solar and heliospheric magnetic fields., PhD Thesis, Stanford University, 1984.
[24]Lee, C. O., et al, Coronal Field Opens at Lower Height During the Solar Cycles 22 and 23 Minimum Periods: IMF Comparison Suggests the Source Surface Should Be Lowered., *Solar Physics*, 269:367-388, 2011.
[25]Riley P., Downs C., Linker J. A., Mikic, Z, Lionello R., Caplan R. M., Predicting the Structure of the Solar Corona and Inner Heliosphere during Parker Solar Probe's First Perihelion Pass., AAS, 874:L15, 2019

[26]Levine, R. H., M. D. Altschuler, J. W. Harvey, and B. V. Jackson, Open magnetic structures on the Sun., *Astrophysical Journal*, Part 1, vol. 215, p. 636-651, 1977.
[27]Kasper, J.C., et al. Solar Wind Electrons Alphas and Protons (SWEAP) Investigation., *Space Sci Rev*, 204: 131, 2016.
[28]McComas et al., Energetic particle environment near the Sun from Parker Solar Probe., *Nature*, this issue, 2019
[29]Belcher, J. W., and Davis, L., Large-amplitude Alfvén waves in the interplanetary medium, 2., *J. Geophys. Res.*, 76 (16), 3534– 3563, 1971
[30]G. G. Howes *et al,* The slow mode nature of compressible wave power in solar wind turbulence., *The Astrophysical Journal Letters* **753** L19, 2012
[31]Horbury et al., Short, large-amplitude speed enhancements in the near-Sun fast solar wind., Monthly Notices of the Royal Astronomical Society, Volume 478, Issue 2, p.1980-1986, 2018
[32]Gosling, J. T., H. Tian, & T. D. Phan, Pulsed Alfven waves in the solar wind., *The Astrophysical Journal Letters* **737**L35, 2011
[33]Balogh, A., R. J. Forsyth, E. A. Lucek, T. S. Horbury, and E. J. Smith, Heliospheric magnetic field polarity inversions at high heliographic latitudes. *Geophys. Res. Lett*., 26, 631– 634, 1999.
[34]Yamauchi, Y., R. L. Moore, S. T. Suess, H. Wang, and T. Sakurai, The magnetic structure of ha macrospicules in solar coronal holes., *Astrophys. J*., 605, 511 – 520, 2004.
[35]Raouafi, N. E. and G. Stenborg, Role of transients in the sustainability of solar coronal plumes., *The Astrophysical Journal*, Volume 787, Issue 2, article id. 118, 11, 2014.
[36]Merrill, R. A. *et al,* Simulated encounters of the Parker Solar Probe with a coronal-hole jet*., The Astrophysical Journal ,***866** 14, 2018.
[37]Meyer-Vernet, N., Issautier, K. & Moncuquet, M. Quasi-thermal noise spectroscopy: the art and the practice., *J. Geophys. Res. Space physics,* **122**, 7925-7945, 2017.
[38]A. A. Schekochihin *et al*, Astrophysical Gyrokinetics: kinetic and fluid turbulent cascades in magnetized weakly collisional plasmas., *ApJS* **182** 310, 2009.
[39]W. H. Matthaeus, M. L. Goldstein, and C. Smith, Evaluation of magnetic helicity in homogeneous turbulence., *Phys. Rev. Lett*. **48**, 1256, 1982.
[40]L. K. Jian *et al*, Electromagnetic waves near the proton cyclotron frequency: STEREO observations., *Astrophysical Journal,* **786** 123, 2014.
[41]Bruno, R. & Carbone, V., The Solar Wind as a Turbulence Laboratory., *Living Rev. Sol. Phys*.,10: 2. https://doi.org/10.12942/lrsp-2013-2, 2013

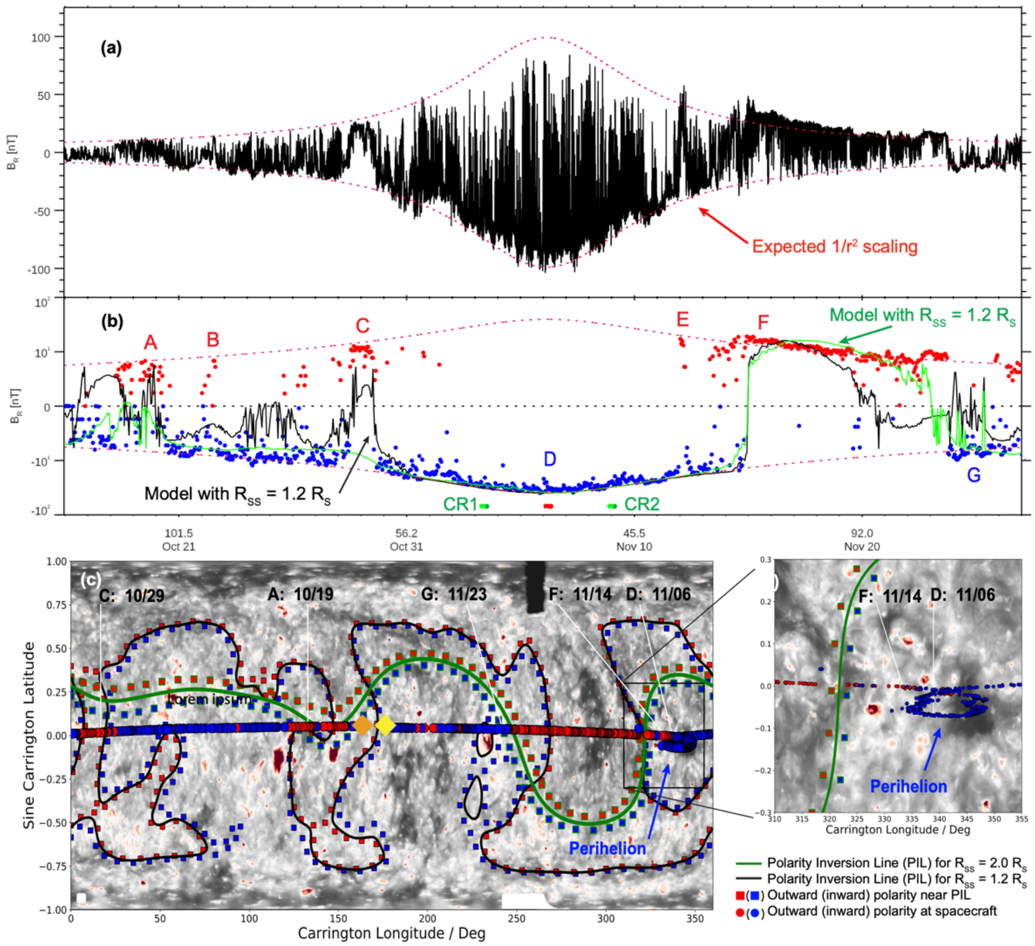


**Fig. 1. Radial magnetic field measurements are highly structured, map back to the Sun, and are consistent with a low source surface. a.** The measured radial magnetic field $B_R$ is comprised of the large-scale field, which scales as ~$1/r^2$ (dotted lines) and rapid, large amplitude, $\delta B_R/|B|$~1 polarity reversals associated with jets of plasma (Fig 2b). **b**. One-hour statistical modes of $B_R$ (on a bi-symmetric log plot) show the large-scale radial field colored for polarity (red=outward, blue=inward). Predicted radial field profiles from a PFSS model are over-plotted using a source surface height $R_{SS}$ = 1.2 $R_S$ (black curve, unscaled) and 2.0 $R_S$ (green curve, multiplied by a factor of 6.5). $R_{SS}$ at 1.2 $R_S$ reproduces many of the measured polarity changes (labeled *A*, *C*, *F*, and G*)*. The $R_{SS}$ = 2.0 $R_S$ model better predicts the timing of polarity inversion *G* (see Methods section). Co-rotation CR1 and CR2 (green) and the perihelion PH (red) at 35.7 $R_S$ are labeled. **c.** An EUV synoptic map of 171Å (Fe IX) emission shows structure associated with active regions and lower density plasma in coronal holes (darker regions). The PSP trajectory at the source surface is superimposed, colored as above for measured field polarity. E1 begins at the orange diamond, moves westward (in decreasing longitude) across the map through perihelion at ~330°, and ends at the yellow diamond. A line shows the location of the model polarity inversion line (PIL) at the source surface ($R_{SS}$ = 1.2 is black, $R_{SS}$ = 2.0 $R_S$ is green). Red and blue colored squares indicate the polarity either side of the PIL models. Red ($B_R > 0$) and blue ($B_R < 0$) lines map the magnetic field from $R_{SS}$ back to the photosphere for $R_{SS}$ = 2.0 $R_S$; for $R_{SS}$ = 1.2 $R_S$ the model field lines are radial. **d.** The EUV map of the perihelion interval showing field lines mapping back to the Sun into a small, equatorial coronal hole, and the location of the adjacent PIL associated with the heliospheric current sheet, from the 2.0 $R_S$ model.

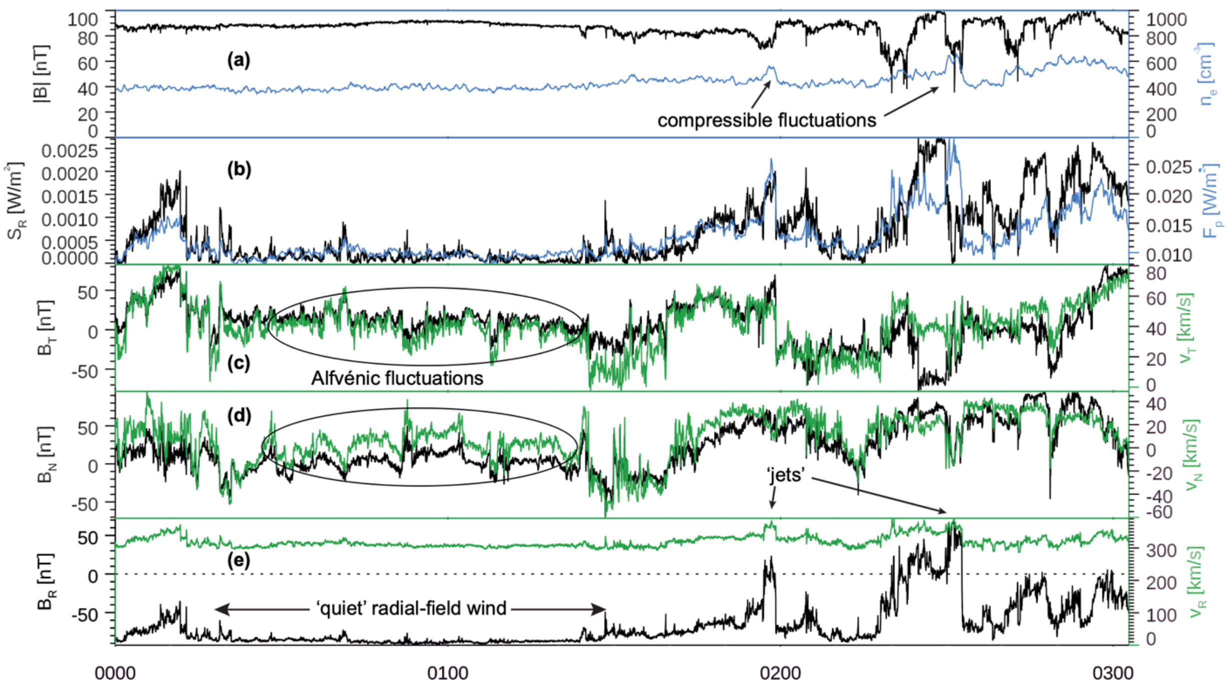


**Fig 2. Magnetic field reversals and plasma jets carry Poynting flux**. **a**. Time series measurements of magnetic field magnitude |B| (black) and total plasma density $n_e$ (blue) show anti-correlation during jet events, consistent with MHD slow-mode behavior. **b.** Radial Poynting flux $S_R$ (black) and ion kinetic energy flux $F_p$ (blue) showing large enhancements during jet/field reversal events. **c.** Tangential (T) component of the magnetic field (black) and plasma velocity (green) components showing Alfvenic fluctuations. **d.** The N component of magnetic field (black) and plasma velocity (green). **e.** Radial magnetic field (black) and plasma velocity (green) showing an interval of quiet, radial field and flow adjacent to magnetic structure associated with jets of plasma. Measurements are made on ~00:00-03:00 on November 5, 2018 at ~36.6 $R_S$. The Alfvén speed during the quiet interval is approximately $v_A$ ~ 100 km/s.

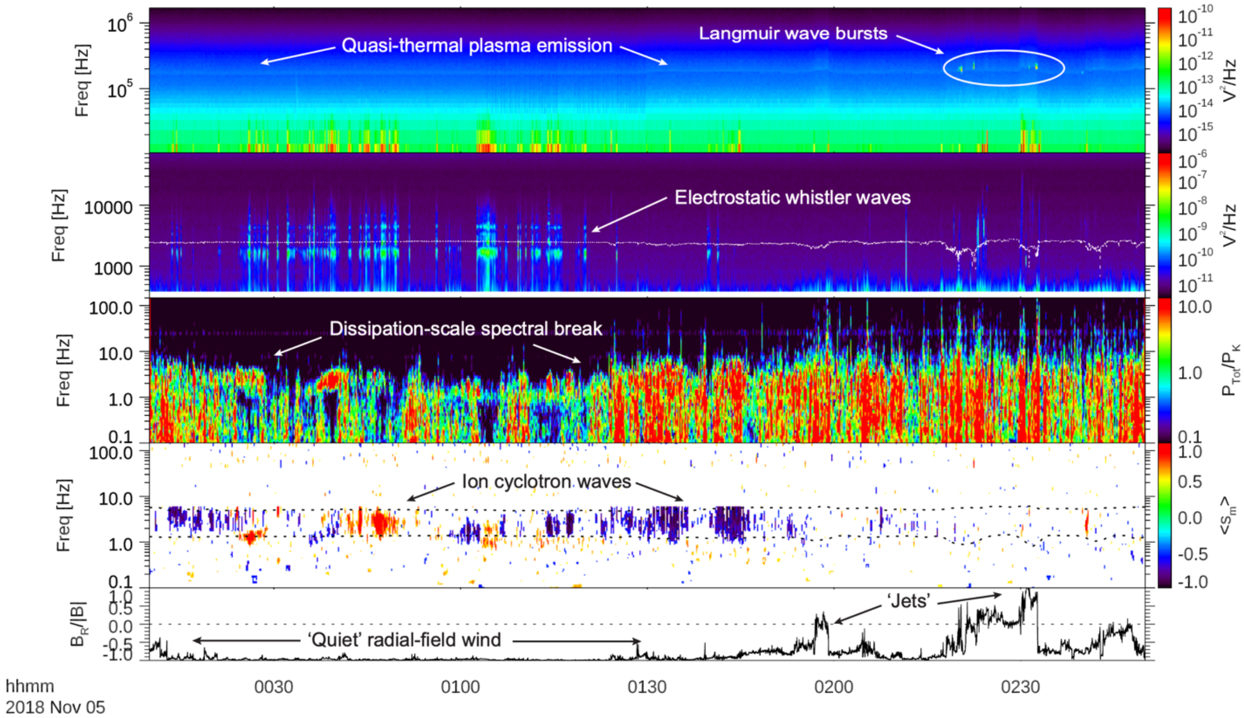


**Fig 3. Plasma wave activity near perihelion differs in quiet wind and jets**. **a.** Spectral density measurements of electric field fluctuations near the electron plasma frequency $f_{pe}$ show intense bursts of electrostatic Langmuir waves with intensities ~$10^2$-$10^4$ $V^2$/Hz above the thermal background, suggesting the presence of electron beams. **b**. Electrostatic waves near the electron cyclotron frequency $f_{ce}$ (white dashed line) and its harmonics are often present in intervals of ambient radial magnetic field, but not jet plasma **c** A wavelet spectrogram of the magnetic field shows bursts of turbulent fluctuations with a distinct spectral break between 1-10 Hz associated with transition to dissipation scales. **d.** Magnetic helicity (from the wavelet spectrogram) shows narrowband $f_{ci} < f < f_{ci} + V_R/V_A$ (the expected Doppler-shifted frequency - dashed lines) signatures associated with ion cyclotron waves, again in quiet radial solar wind. **e.** The normalized radial magnetic field $B_R/|B|$ shows distinct intervals of quiet wind with radial field, reduced turbulent levels, and enhanced occurrence of electrostatic whistler and ion cyclotron instability. Measurements are made on ~00:00-03:00 on November 5, 2018 at ~36.6 $R_S$.

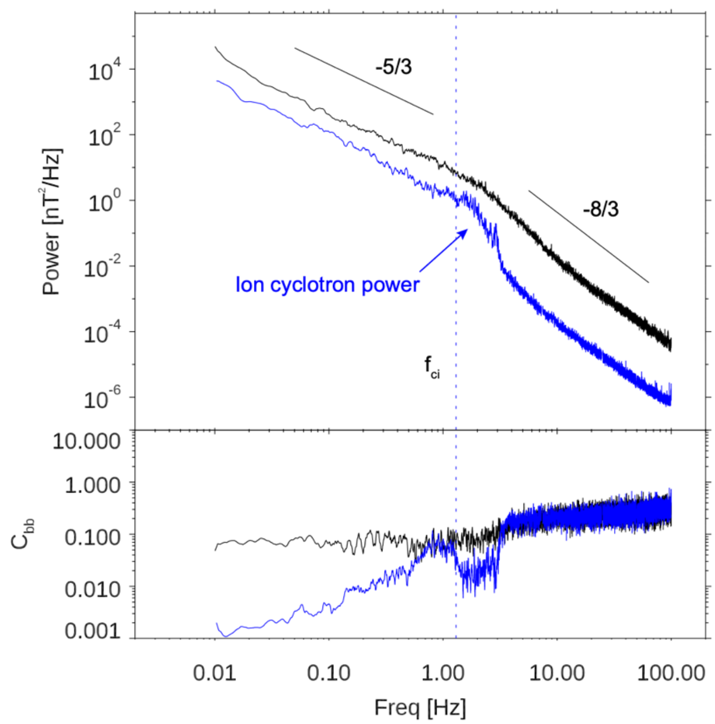


**Fig 4. Power spectral density and magnetic compressibility of magnetic field fluctuations in quiet and jet wind.** Thirty-minute integrated power spectra of fluctuations in quiet (blue) and jet (black) solar wind conditions show the transition from MHD inertial range to dissipation and/or dispersion range turbulence, here compared to spacecraft-frame frequency $f^{-5/3}$ and $f^{-8/3}$ power laws (upper panel). The quiet wind spectrum (blue) shows enhanced power at near the ion cyclotron frequency ($f_{ci}$) associated with enhanced magnetic helicity (Fig. 3e). The ratio of magnitude (|B|) to Trace (B) spectra (lower panel) indicates enhanced magnetic compressibility during jet intervals (black) compared to quiet wind (blue) up to the dissipation scale (-8/3 slope). The ion cyclotron band corresponds to lower compressibility, as expected.

# Methods

**Heliocentric RTN Coordinates:** We use so-called Heliocentric RTN coordinates in our study, which are defined as follows: R points from the Sun center to the spacecraft. T lies in the spacecraft plane (close to the ecliptic) and is defined as the cross product of the solar rotation axis with R and points in the direction of prograde rotation. N completes a right-handed system.

**Statistical Modes:** To examine the large-scale magnetic structure, (Fig. 1b) we seek to remove the rapidly varying spikes observed in Fig. 1a. To do this we produce statistical modes which are defined by binning the full cadence magnetic field observations into 1-hour intervals and for each interval, calculating the modal value - the peak of the histogram of field values within each interval.

**Identification of Jet Intervals**: In the main text we state that approximately 6% of the duration of E1 consists of jet intervals. That number is computed by measuring the duration of positive polarity $B_R$ intervals (58973 seconds) occurring from October 30, 2018 to November 11, 2018 (1036800 seconds total). This interval was chosen to correspond to interval *D*, of primarily negative polarity, in Fig. 1b over the coronal hole, and without transient coronal mass ejection events. The positive polarity jets were identified using a simple zero-crossing algorithm applied to 1 second cadence radial magnetic field data $B_R$. Of course, not all so-called 'jets' contain full polarity reversals. Biasing this calculation with an amplitude offset will produce a larger fraction of jet times; this is an ongoing study.

**PSP/FIELDS Measurement Details**: Measurements presented in the main text were made by the FIELDS[17] and SWEAP[27] instruments on the PSP spacecraft. Magnetic field measurements in Fig. 1a are made by the FIELDS fluxgate magnetometer and are averaged to 1 second cadence, from their native cadence which varies from ~2.3 to 293 samples per second over E1. The $B_R$ data shown in Fig. 1b is derived from the 1 second data by then computing the distribution of amplitudes in one-hour intervals, with amplitude resolution of 1 nT, and finding the peak value of that distribution: the statistical mode. This technique removes the fluctuating 'jet' intervals, without introducing the amplitude bias of an averaging algorithm.
The magnetic field measurements in Fig. 2 start at 1 second cadence, averaged down from their native cadence as described above. All magnetic field measurements here are calibrated accurate to better than 0.5 nT. SWEAP velocity measurements are made by the Solar Probe Cup (SPC) sensor at a cadence of ~1 measurement per 0.87 sec and then averaged to 5 second intervals. The 1 second cadence magnetic field data is then averaged onto these 5 second time intervals. This reduces fluctuation noise in the SPC data and provides velocity and magnetic field measurements at the same cadence. The plasma density measurements in Fig. 1a are made using the FIELDS Low Frequency Receiver (LFR)[42], which measures the fluctuating electric field across the V1-V2 antenna pair[17] and computes spectral density (also shown in Fig. 3a). The spectral peak is identified and associated with the electron plasma frequency $f_{pe}$, as described in Meyer-Vernet et al.[25], hence the frequency of the peak amplitude gives a reliable estimate of the total plasma density. The spectral resolution of the LFR instrument is $\Delta f/f \approx 4\%$. The plasma frequency $f_{pe}$ is proportional to $\sqrt{n_e}$, where $n_e$ is electron (total) density; therefore the resulting uncertainty in the density measurement is $\Delta n/n \approx 2\ \Delta f/f \approx 8\%$. Electric field measurements used to compute the radial Poynting flux in Fig. 2b are measured directly as differential voltage pairs[43] between V1-V2 and V3-V4 antennas[17] and then calibrated to electric field units by comparison to $-\mathbf{v} \times \mathbf{B}$ computed from the SPC velocity and fluxgate magnetometer data. This allows us to remove spacecraft offset electric fields and compute an effective probe separation length, a standard technique used to calibrate electric field instrumentation[44]. The electric field measurement is accurate to approximately 1 mV/m.
Measurements in Fig. 3a show the full spectrum of the RFS/LFR[42] receiver, in spectrogram form, measured on the V1-V2 antenna pair. Wave intensity in Fig. 3a ranges from ~6 $10^{-17}$ to 1.4 $10^{-10}$ $V^2$/Hz and is represented logarithmically. The spectral bandwidth of the LFR receiver is $\Delta f/f = 4.5\%$ and the cadence of the measurement is 1 spectrum each ~7 seconds. Fig. 3b shows the electric field spectrogram of differential voltage measurements on the V1-V2 antenna pair from the Digital Fields Board (DFB) subsystem[43], with intensity in arbitrary log amplitude units. DFB 'AC' spectral resolution is $\Delta f/f$ ~6-12% and the measurement cadence is 1 spectrum per 5.5 seconds. Fig. 3c shows the magnetic field spectrogram of search coil magnetometer

measurements on the from the Digital Fields Board (DFB) subsystem[43], with intensity in arbitrary log amplitude units. DFB 'DC' spectral resolution is $\Delta f/f$ ~6-12% and the measurement cadence is 1 spectrum per 28 seconds. The wavelet spectrogram in Fig. 3d and magnetic helicity spectrum in Fig. 3e were computed using the 'wav_data' IDL routine in SPEDAS[42] suite of IDL analysis routines. Wave intensity in Fig. 3d is represented in log power in arbitrary units and is divided by a factor $P_K \sim f^{-5/3}$ (flattened), so that a power spectrum with spectral index -5/3 would have no frequency dependence.

**PFSS modeling and connection to Parker Solar Probe:** Modeling the magnetic field time series (Fig 1. Panel (b)) and tracing field lines from Parker Solar Probe down into the corona (Fig 1. panels (c,d)) was performed with 2 main steps :

(1) *PFSS Implementation* **:** PFSS[19,20,9] modeling used the recent open source python implementation *pfsspy*[46,47]. This code package is freely available online, extremely flexible with regard to changing the input parameters, and efficient (a full PFSS solution can be extracted in ~14 seconds including downloading the magnetogram on demand). Given a magnetogram and source surface height (RSS) as boundary conditions, the code solves the Laplace equation (Equation 1) for the magnetic scalar potential and outputs a full 3D magnetic field within the annular volume bounded by the photosphere and the source surface parameter. The choice of magnetogram data and values of source surface height depicted in figure 1 and discussed further below.

$$\nabla^2 \, \Phi_B(r) = 0 \qquad \text{(Equation 1)}$$

*(2) Ballistic Propagation :* The procedure to magnetically connect PSP to a particular location at the outer boundary of the PFSS solution domain follows Nolte & Roelof[48,49, 50], where the field line intersecting the position of PSP is assumed to follow a Parker spiral[1] with a curvature determined by the co-temporal solar wind velocity measurement at that position. As discussed by Nolte & Roelof[48], while at lower radii this approximation is strongly perturbed by both corotational effects and the acceleration of the solar wind, these effects actually shift the coronal longitude by a similar magnitude but in opposite directions resulting in an estimated error in longitude less than 10 degrees. This produces a very simple mapping (Equation 2) from spacecraft spherical Carrington coordinates ($r_{PSP}$, $\theta_{PSP}$, $\phi_{PSP}$) down to coordinates on the source surface (r, θ, ϕ) which involves $\Omega_S$, the solar sidereal rotation rate and $v_R$, the measured solar wind speed:

$$\begin{pmatrix} r \\ \theta \\ \phi \end{pmatrix} = \begin{pmatrix} R_{SS} \\ \theta_{PSP} \\ \phi_{PSP} + \frac{\Omega_S}{v_R}(r_{PSP} - R_{SS}) \end{pmatrix} \qquad \text{(Equation 2)}$$

To generate time series predictions, we first download a magnetogram, choose a source surface height and generate a PFSS solution with (1). We then take PSP's trajectory and use (2) to produce a time series of latitudes and longitudes on the source surface to which PSP was connected to (see red and blue trajectory in Figure 1 (c,d) and Extended Data Figures 1-3). For each latitude and longitude we obtain a $B_R$ value at the source surface from the PFSS model.

Finally, we scale each $B_R$ value by C $(R_{SS}/r_{PSP})^2$ to produce an estimate of BR at PSP's location as a function of time. C is an empirically determined constant used to scale the time series prediction to match the peak measured magnetic field. Its value is dependent on the choice of magnetogram but also approaches unity as the source surface height decreases and more flux is opened to the heliosphere. For the model results shown in Figure 1, the values of C are 6.7 (2.0 Rs model) and 1.4 (1.2 Rs model). To produce field line traces and generate Fig 1. (c,d), we start with the time series of latitudes and longitudes on the source surface connected to PSP. For each pair of coordinates, we use *pfsspy*'s built-in field line tracer. Given the output of the *pfsspy* model, we supply the source surface latitudes and longitudes and the field line tracer generates a field line which starts from that point and propagates it down to the photosphere. The model also provides a polarity for each field line generated which we use to colorize the field lines which we plot in Fig 1. (c,d).

**Choice of Magnetogram Data and Source Surface Height for Figure 1:** Synoptic maps of the photospheric magnetic field are available from multiple sources which can cause variation in PFSS model output. In this work we consider the NSO/GONG zero-point corrected data product[51], SDO/HMI vector magnetogram data product[52], and the DeRosa (LMSAL) modeled magnetogram[53]. GONG has the advantage of being operationally certified for space weather predictions, SDO/HMI is space-based and offers better resolution, while the DeRosa model assimilates HMI data, uses a surface flux transport and far-side helioseismological data to far side simulate photospheric dynamics such as differential rotation. Additional variation arises from time evolution of the photospheric observations. Synoptic magnetograms are built by many observations of the Sun from Earth as it rotates with a ~27 day period. Typically, only ± 60 degrees longitude about the central meridian (sub-Earth point) are used for each observation (grey regions in Extended Data Fig 1-3). While these maps can be updated with new data as frequently as observations are made, portions of the Sun facing away from Earth cannot be updated until they rotate into view, meaning all synoptic maps consist of a mix of old and new data and evolve in time. Finally, the model output depends significantly on the choice of the source surface height parameter (RSS). The inferred structure at the source surface changes as the source surface is lowered: Implied structure such as the polarity inversion line (PIL) - contour of BR = 0 - becomes more structured and warped. The footpoints of open field lines at the photosphere encompass larger areas, increasing the predicted size of coronal holes and the total amount (both positive and negative) of magnetic flux crossing the source surface increases. Our approach to make robust conclusions is to generate model results for multiple times from all three magnetogram sources for varying source surface heights. Color maps of Br at the source surface and the associated PILs are shown in Extended Data Figures 1-3. The majority of models at 2.0 Rs and below predict polarity inversions in the vicinity of 240° and 310° longitude at all source surface heights, with additional polarity inversions around 10° and 140° longitude developing at lower source surface height. These features are all consistent with PSP measurements and we highlight that they are largely independent of time of observation and choice of magnetogram source. While the canonical[23] 2.5 Rs value still gives good results from a GONG evaluation, both HMI and the DeRosa models produce strong disagreement around the time of perihelion. In Figure 1 (b-d) we show results from the Gong zero-point corrected map evaluated on 11/06/2018 about which our time range of analysis is symmetric. This evaluation shows all the above features and produce good time series agreements. We show source surface heights of 2.0 Rs and 1.2 Rs. These lower source surface heights do have modern precedent: The

2.0 Rs is consistent with PFSS modeling done for the same interval by Riley et al.[25], where they chose this height to better match the observed extent of coronal holes. Lee et al[24] also investigated the impact of lowering the source surface height on model results, observing at solar minimum a lower (<2.0 Rs) source surface height was required to populate equatorial coronal holes with open field lines and improve estimates of magnetic field strength at 1 AU.

## Additional References for Methods:


[42]Pulupa, M., et al., The Solar Probe Plus Radio Frequency Spectrometer: Measurement requirements, analog design, and digital signal processing., *J. Geophys. Res. Space Physics*, 122, 2836– 2854, 2017

[43]Malaspina, D. M., et al., The Digital Fields Board for the FIELDS instrument suite on the Solar Probe Plus mission: Analog and digital signal processing., *J. Geophys. Res. Space Physics*, 121, 5088– 5096, 2016

[44]Mozer, F. S., DC and low-frequency double probe electric field measurements in space., *J. Geophys. Res. Space Physic*s, 121, 10,942–10,953, 2016.

[45]Angelopoulos, V. et al., The Space Physics Environment Data Analysis System (SPEDAS)., *Space Science Reviews*, v215, id 9, 2019.

[46]Stansby, D., Dstansby/pfsspy: Pfsspy 0.1.2 zenodo, 2019.

[47]Yeates, A., Antyeates1983/pfss: First release of pfss code zenodo, 2018.

[48]Nolte, J. T. and E. C. Roelof, Large-Scale Structure of the Interplanetary Medium, I: High Coronal Source Longitude of the Quiet-Time Solar Wind., *Solar Physics*, 33:241-257, November 1973.

[49]Neugebauer, M., et al, Spatial structure of the solar wind and comparisons with solar data and models., *Journal of Geophysical Research: Space Physics*, 103(A7):14587-14599, 7 1998.

[50]Stansby, D., T. S. Horbury, S. Wallace, and C. N. Arge, Predicting large-scale coronal structure for Parker Solar Probe using open source software., *Research Notes of the AAS*, 3(3):57, mar 2019.

[51]Clark, R., J. Harvey, F. Hill, and C. Toner, GONG Magnetogram Zero-Point Correction Status., In AAS/Solar Physics Division Meeting #34, volume 35 of *Bulletin of the American Astronomical Society*, page 822, May 2003

[52]Hoeksema, J. T., et al, The Helioseismic and Magnetic Imager (HMI) Vector Magnetic Field Pipeline: Overview and Performance., *Solar Physics*, 289(9):3483-3530, Sep 2014.

[53]Schrijver, C. J. and M. L. DeRosa, Photospheric and heliospheric magnetic fields., *Solar Physics*, 212: 165, 2003.

**Acknowledgements.** The FIELDS experiment on the Parker Solar Probe spacecraft was designed and developed under NASA contract NNN06AA01C. The FIELDS team acknowledges the contributions of the Parker Solar Probe mission operations and spacecraft engineering teams at the Johns Hopkins University Applied Physics Laboratory. S.D.B. acknowledges the support of the Leverhulme Trust Visiting Professorship program. Contributions from S.T.B. were supported by NASA Headquarters under the NASA Earth and Space Science Fellowship Program Grant 80NSSC18K1201. This work utilizes data obtained by the Global Oscillation Network Group (GONG) Program, managed by the National Solar Observatory, which is operated by AURA, Inc. under a cooperative agreement with the National Science Foundation. The data were acquired by instruments operated by the Big Bear Solar Observatory, High Altitude Observatory, Learmonth Solar Observatory, Udaipur Solar Observatory, Instituto de Astrofísica de Canarias, and Cerro Tololo Interamerican Observatory. D. B. was supported by UK STFC grant ST/P000622/1. J. P. E. and T. S. H. were supported by UK STFC grant ST/S000364/1. D. S. was supported by UK STFC grant ST/N000692/1. CHKC is supported by STFC Ernest Rutherford Fellowship ST/N003748/2. T.D. and V.K. are supported by CNES.

**Author Contributions.** S.D.B. wrote the manuscript with substantial contributions from S.T.B., B.D.G.C., C.H.K.C., T.S.H., M.M., T.D.P. and M.V. All authors participated in the data interpretation, read and commented upon the manuscript. S.D.B. led the FIELDS instrument team with contributions from J.W.B., T.A.B, T.D., K.G., P.R.H., D.E.L., R.J.M., M.M, D.M.M., M.P, and N.E.R.

**Competing Interests.** The authors declare no competing interests.

**Correspondence and requests for materials** should be addressed to S.D.B.



## Extended Data

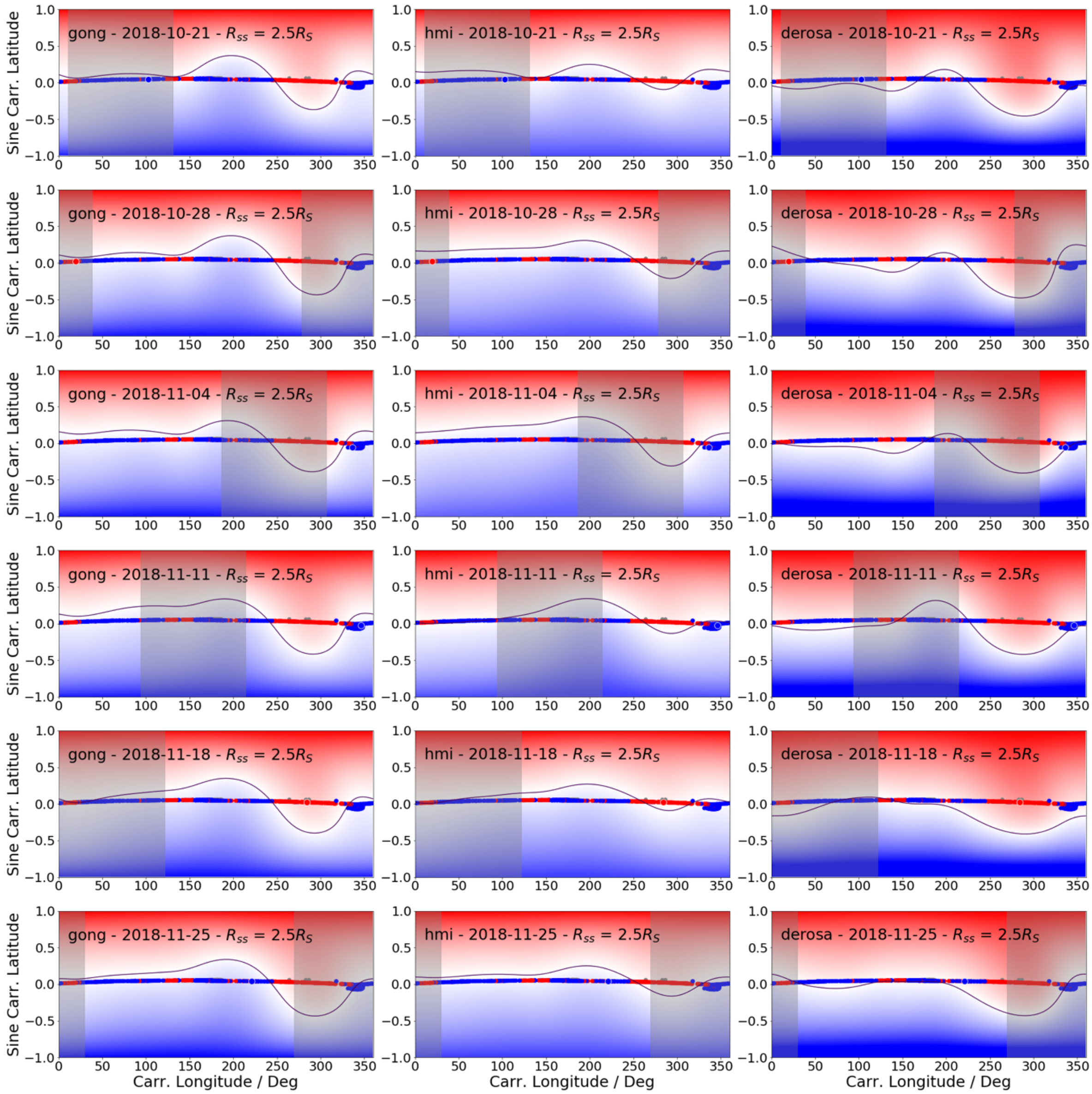


**Extended Data Figure 1: Variation of PFSS Neutral Line topology with time and magnetogram choice at 2.5 Rs Source Surface Radius**. Colormaps of $B_r$ at the source surface of PFSS extractions with Source Surface radius $R_{SS}$ = 2.5 $R_S$. Red indicates positive polarity, while blue indicates negative. The black line shows the polarity inversion line (contour of $B_R$ = 0). Superposed is the ballistically projected PSP trajectory colored by the measured polarity. Perihelion occurred around 330 longitude. Left to right, the columns show extractions from NSO/GONG, SDO/HMI and the DeRosa LMSAL Model. From top to bottom, the models are evaluated at a weekly cadence spanning 6 weeks about perihelion, with input magnetograms from each source taken as close in time as possible. The grey shading shows +/-60 degrees about the central meridian on date of model evaluation indicating the portion of the Sun that could be observed at the time of observation.

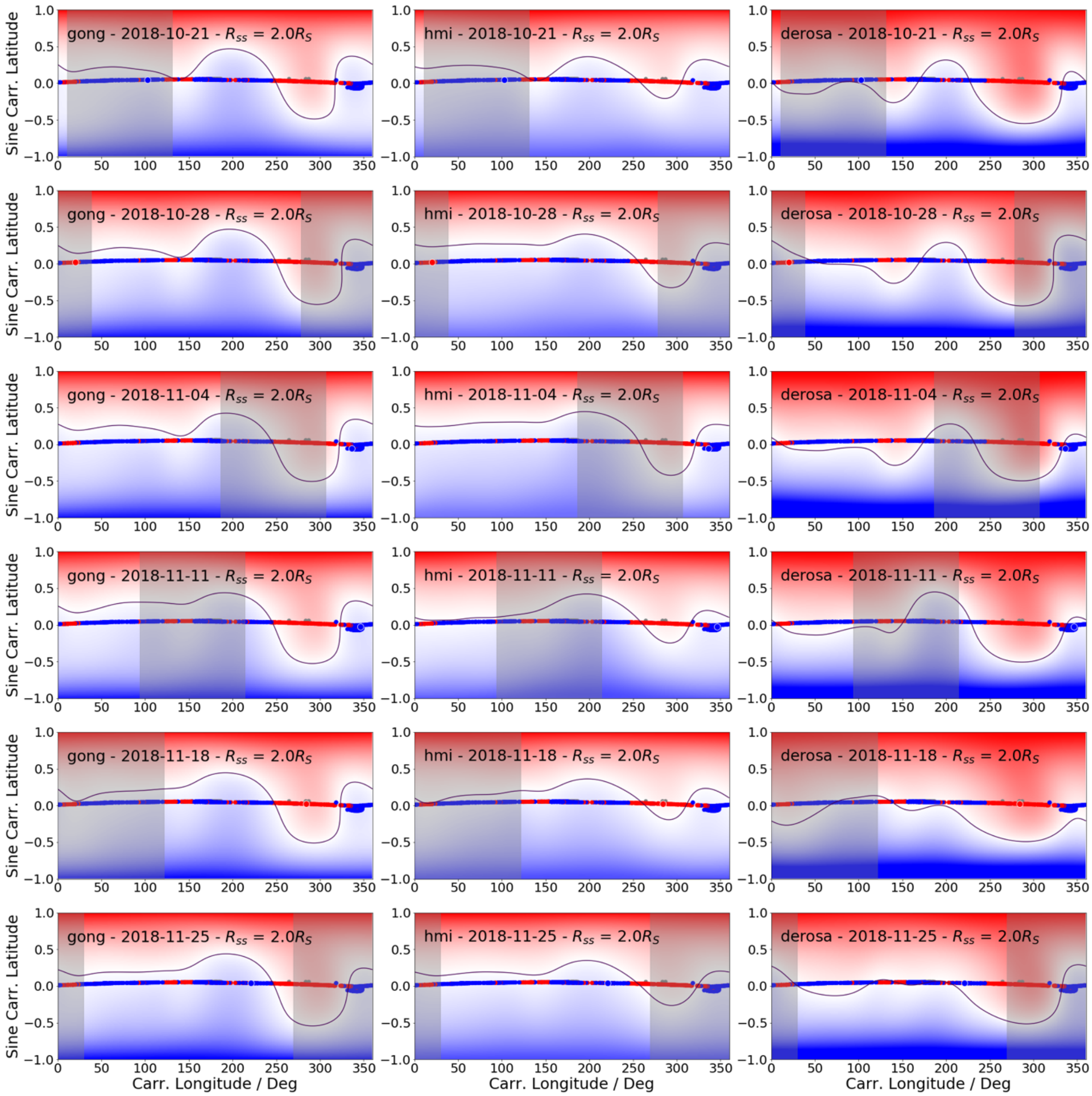


**Extended Data Figure 2: Variation of PFSS Neutral Line topology with time and magnetogram choice at 2.0 Rs Source Surface Radius**. Colormaps of $B_r$ at the source surface of PFSS extractions with Source Surface radius $R_{SS}$ = 2.0 $R_S$. Red indicates positive polarity, while blue indicates negative. The black line shows the polarity inversion line (contour of $B_R$ = 0). Superposed is the ballistically projected PSP trajectory colored by the measured polarity. Perihelion occurred around 330° longitude. Left to right, the columns show extractions from NSO/ GONG, SDO/HMI and the DeRosa LMSAL Model. From top to bottom, the models are evaluated at a weekly cadence spanning 6 weeks about perihelion, with input magnetograms from each source taken as close in time as possible. The grey shading shows +/-60 degrees about the central meridian on date of model evaluation indicating the portion of the Sun that could be observed at the time of observation.

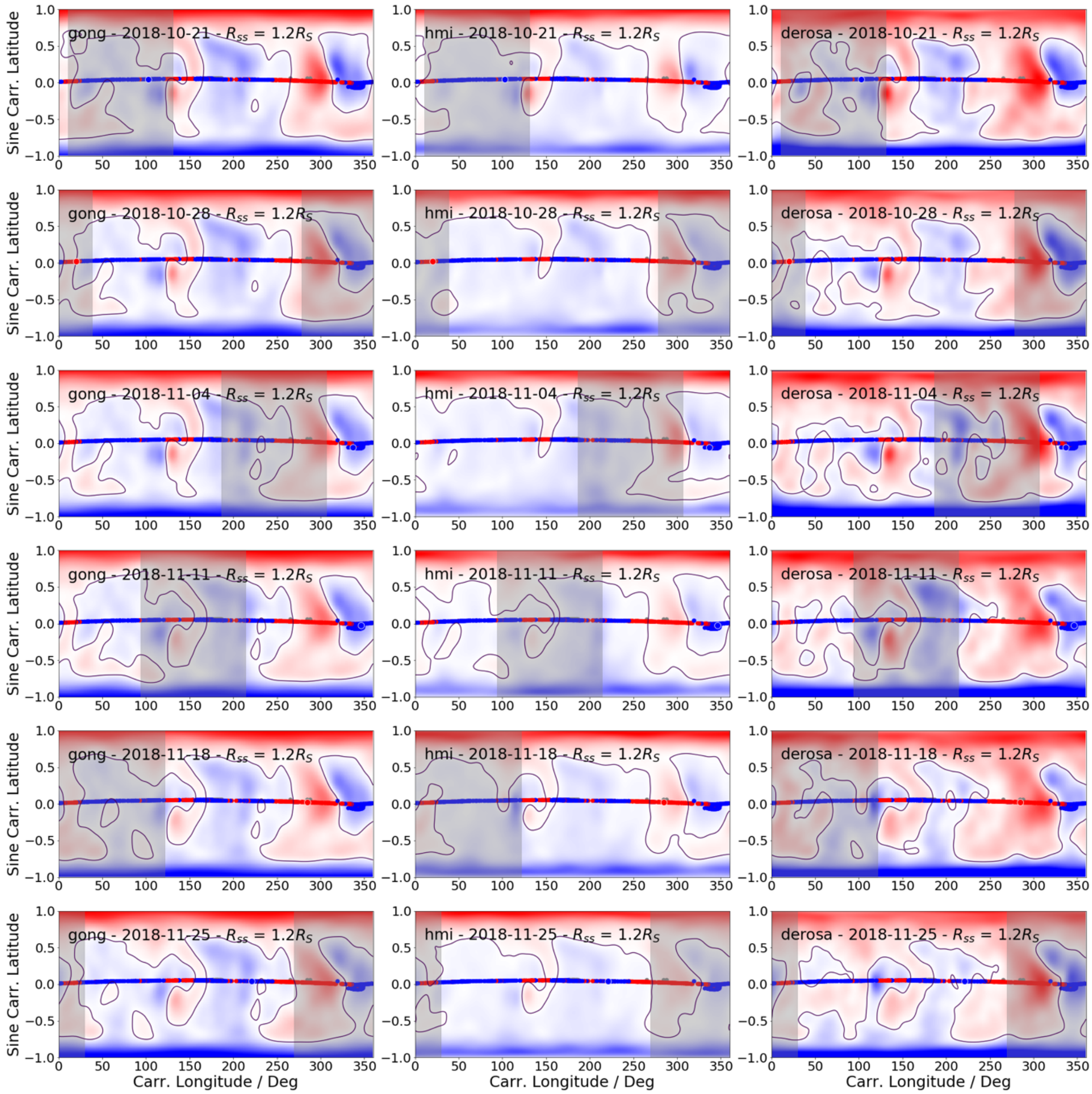


**Extended Data Figure 3: Variation of PFSS Neutral Line topology with time and magnetogram choice at 1.2 Rs Source Surface Radius.** Colormaps of $B_r$ at the source surface of PFSS extractions with Source Surface radius $R_{SS}$ = 1.2 $R_S$. Red indicates positive polarity, while blue indicates negative. The black line shows the polarity inversion line (contour of $B_R$ = 0). Superposed is the ballistically projected PSP trajectory colored by the measured polarity. Perihelion occurred around 330° longitude. Left to right, the columns show extractions from NSO/ GONG, SDO/HMI and the DeRosa LMSAL Model. From top to bottom, the models are evaluated at a weekly cadence spanning 6 weeks about perihelion, with input magnetograms from each source taken as close in time as possible. The grey shading shows +/-60 degrees about the central meridian on date of model evaluation indicating the portion of the Sun that could be observed at the time of observation.

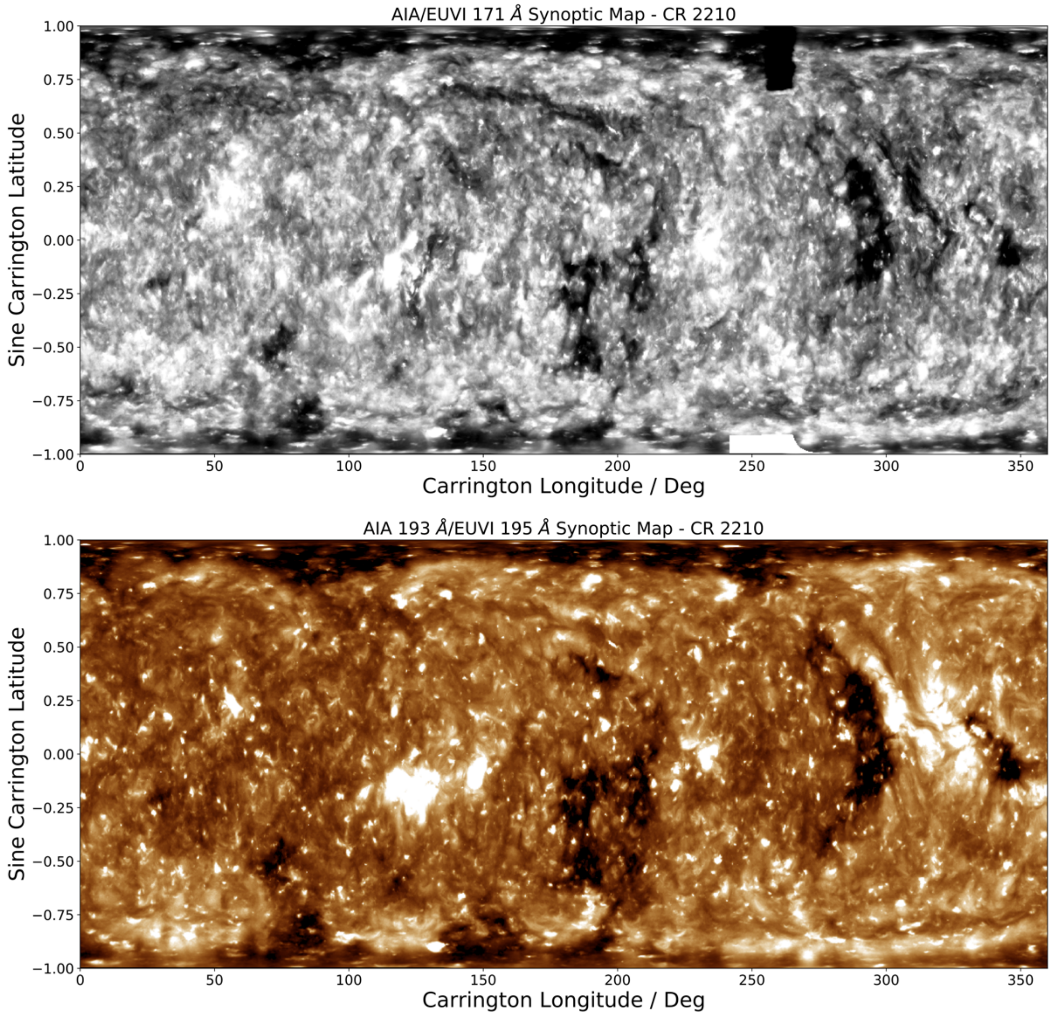


**Extended Data Figure 4. Synoptic maps of Extreme Ultraviolet (EUV) coronal emission from Carrington Rotation 2210 assembled from the STEREO A/EUVI and SDO/AIA instruments**. Top: 171 Å data showing coronal Iron-9 emission from ~600 000 K. This is the background the Figure 1. Panels (c), (d). Bottom: 193Å (AIA)/ 195Å (EUVI) data showing emission from coronal Iron-12 emission at 1000000 K. Brightness is positively correlated the integrated plasma density squared along the line of sight. Dark regions in both images are likely locations of coronal holes which are threaded by open magnetic field lines which allow plasma to evacuate into interplanetary space and hence result in under-dense regions.

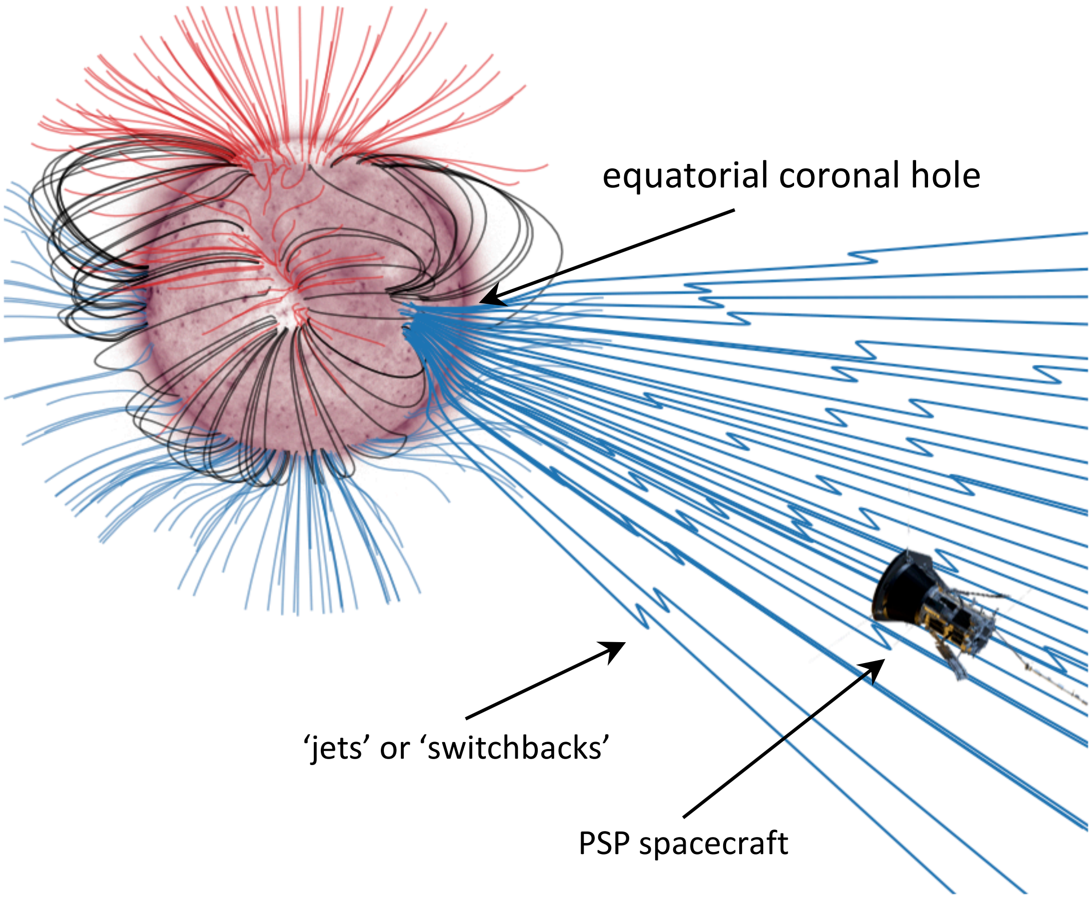


**Extended Data Figure 5. During encounter 1, Parker Solar Probe (PSP) connects magnetically to a small, negative polarity equatorial coronal hole.** This schematic shows a potential field extrapolation of the solar magnetic field at the time of the first perihelion pass of PSP. The solar surface is shown colored by AIA 211Å extreme ultraviolet emission (see Extended data figure 4 for other EUV wavelengths). Coronal holes appear as a lighter shade. Superposed are various field lines initialized at the solar disk. Black lines indicate closed loops, blue and red illustrate open field lines with negative and positive polarities respectively. As depicted here, and in Figure 1(c), (d), at perihelion PSP connected to a negative equatorial coronal hole. The "switchbacks" (jets) observed by PSP (Figure 1(a)) are illustrated as kinks in the open field lines emerging from this coronal hole and connecting to PSP. (Note the neither the radial distance to the spacecraft nor the scale/amplitude of the jets/switchbacks are to scale.) Spacecraft image is courtesy of NASA/Johns Hopkins APL.